

Gradual transition from insulator to semimetal of $\text{Ca}_{1-x}\text{Eu}_x\text{B}_6$ with increasing Eu concentration

R.R. Urbano¹, P.G. Pagliuso¹, C. Rettori¹, P. Schlottmann², J.L. Sarrao³,

A. Bianchi³, S. Nakatsuji^{2,4}, Z. Fisk^{2,5}, E. Velazquez⁶ and S.B. Oseroff⁶

¹ Instituto de Física "Gleb Wataghin", UNICAMP, Campinas-SP, 13083-970, Brazil.

² Department of Physics and National High Magnetic Field Laboratory,
Florida State University, Tallahassee, FL 32306, U.S.A.

³ Los Alamos National Laboratory, Los Alamos, New Mexico 87545, U.S.A.

⁴ Department of Physics, University of Kyoto, Kyoto 606-8502, Japan

⁵ Department of Physics, University of California, Davis, CA 95616, U.S.A.

⁶ San Diego State University, San Diego, California 92182, U.S.A.

(Dated: November 5, 2018)

The local environment of Eu^{2+} ($4f^7, S = 7/2$) in $\text{Ca}_{1-x}\text{Eu}_x\text{B}_6$ ($0.003 \leq x \leq 1.00$) is investigated by means of electron spin resonance (ESR). For $x \lesssim 0.003$ the spectra show resolved *fine* and *hyperfine* structures due to the cubic crystal *electric* field and nuclear *hyperfine* field, respectively. The resonances have Lorentzian line shape, indicating an *insulating* environment for the Eu^{2+} ions. For $0.003 \lesssim x \lesssim 0.07$, as x increases, the ESR lines broaden due to local distortions caused by the Eu/Ca ions substitution. For $0.07 \lesssim x \lesssim 0.30$, the lines broaden further and the spectra gradually change from Lorentzian to Dysonian resonances, suggesting a coexistence of both *insulating* and *metallic* environments for the Eu^{2+} ions. In contrast to $\text{Ca}_{1-x}\text{Gd}_x\text{B}_6$, the *fine* structure is still observable up to $x \approx 0.15$. For $x \gtrsim 0.30$ the *fine* and *hyperfine* structures are no longer observed, the line width increases, and the line shape is purely Dysonian anticipating the *semimetallic* character of EuB_6 . This broadening is attributed to a spin-flip scattering relaxation process due to the exchange interaction between conduction and Eu^{2+} $4f$ electrons. High field ESR measurements for $x \gtrsim 0.15$ reveal smaller and anisotropic line widths, which are attributed to magnetic polarons and Fermi surface effects, respectively.

PACS numbers: 71.10.Ca, 71.35.-y, 75.10.Lp

I. INTRODUCTION

The system $\text{Ca}_{1-x}\text{R}_x\text{B}_6$ (R = rare-earths, specially La) has become the focus of extensive scientific investigations since weak-ferromagnetism (WF) at high-temperature ($T_c \approx 600 - 800$ K) has been reported in these materials by Young *et al.*[1] Over the last few years, enormous efforts were devoted, both theoretically [2, 3, 4, 5, 6, 7, 8] and experimentally, [1, 9, 10, 11, 12, 13, 14, 15, 16, 17] to establish the origin of the WF in $\text{Ca}_{1-x}\text{La}_x\text{B}_6$ and its relationship with the actual conducting nature of R doped CaB_6 . However, the nature of the WF of the parent compound CaB_6 is still controversial. Studies of the de Haas-van Alphen effect,[10, 11] the plasma edge in optical spectroscopy,[12, 13] and some electrical resistivity measurements [18] support a semimetallic character for CaB_6 , whereas NMR,[14] thermopower,[15] angle-resolved photoemission (ARPES),[16] and a different set of resistivity measurements [12, 17] suggest that CaB_6 is a well defined semiconductor. High-resolution ARPES by Souma *et al.* [18] revealed an energy gap of about 1 eV between the valence and conduction bands and a carrier density of the order of $5 \times 10^{19} \text{ cm}^{-3}$ for their CaB_6 single crystals. Vonlanthen *et al.* [12] reported that, depending on the crystal growth method, undoped CaB_6 can also show WF. They argue that self-doping attributed to defects might occur. Terashima *et al.*[19] reported that data for $\text{Ca}_{0.995}\text{La}_{0.005}\text{B}_6$ is strongly sample dependent

and, lately, doubts about the intrinsic nature of the WF in these systems are being raised.[20] It has also been argued that CaB_6 is a ~ 1 eV-gap semiconductor and that the intrinsic WF could be hidden by the ferromagnetism (FM) of Fe and Ni impurities at the surface of the crystals.[21]

The electron spin resonance (ESR) study on Gd^{3+} in $\text{Ca}_{1-x}\text{Gd}_x\text{B}_6$ by Urbano *et al.*[9] has shown that the doping process in this compound leads to an inhomogeneous material. Coexistence of *metallic* and *insulating* local environments for Gd^{3+} were observed for Gd concentrations of ~ 1000 ppm.[9] No evidence of WF was found in the Gd^{3+} ESR spectra of either *metallic* or *insulating* regions. Nonetheless, some of the crystals displayed a $g \sim 2.00$ narrow ($\Delta H \approx 10$ Oe) resonance, which disappeared after a gentle etching of the sample. These results suggest that the Gd^{3+} $4f$ -electrons are shielded from the WF field, i.e. the WF might be confined to small regions or to the surface of the sample away from the impurity R sites. In addition, for Gd concentrations $\gtrsim 2000$ ppm, an intriguing collapse of the cubic crystal field (CF) *fine* structure was observed in the ESR spectra of Gd^{3+} ions in the *metallic* regions.[9]

In contrast to CaB_6 , EuB_6 is a well established *semimetallic* material that orders ferromagnetically at $T_c \approx 15$ K,[17, 22, 23] although recently Wigger *et al.* [24] interpreted their EuB_6 data in the framework of a small-gap semiconductor. The electronic configuration of Eu^{2+} ions ($4f^7, S = 7/2$) is identical to that of the Gd^{3+}

ions. However, the effect of Gd^{3+} and Eu^{2+} doping in CaB_6 is quite different since Eu^{2+} has the same valence as Ca^{2+} , while Gd^{3+} delivers an extra electron to the system creating a hydrogen-like donor state with large Bohr radius. The *insulator to metal* transition revealed by the change in the ESR line shape is then reached when the Gd donor bound-states overlap and start to form a *percolative* network. Since not all Gd-sites participate in this network, a coexistence of *metallic* and *insulating* local environments are observed for Gd concentrations of ~ 1000 ppm.

The substitution of Ca^{2+} by Eu^{2+} impurities does not yield a donor bound state. Instead, the broken translational invariance of the lattice introduces a localized split-off state from the valence/conduction band. The energy of such state lies in the gap of the semiconductor and its spatial extension is of the order of one unit cell. Thus an impurity band for Eu^{2+} only forms at much higher concentrations than for Gd^{3+} , as it is indeed observed in our experiments.

Therefore, an ESR study, probing the local Eu^{2+} environment in $\text{Ca}_{1-x}\text{Eu}_x\text{B}_6$, is of great interest to understand the magnetic/non-magnetic and metallic/non-metallic properties of these materials. In this work we present a systematic Eu^{2+} ESR study of $\text{Ca}_{1-x}\text{Eu}_x\text{B}_6$ single crystals for $0.003 \leq x \leq 1.00$. Preliminary X band data in some of these samples were already presented previously.[25] For EuB_6 ($x = 1.00$) Urbano *et al.*[26] have recently attributed the broad line width observed in their ESR experiments to a spin-flip scattering relaxation process due to the exchange interaction between the $\text{Eu}^{2+} 4f$ and conduction electrons. As a consequence, the observed field, temperature, and angular dependence of the ESR line width could be associated with the Fermi surface of the conduction states and the formation of magnetic polarons.

II. EXPERIMENTS

Single crystals of $\text{Ca}_{1-x}\text{Eu}_x\text{B}_6$ ($0.003 \leq x \leq 1.00$) were grown as described in Ref. [1]. The structure and phase purity were checked by x-ray powder diffraction and the crystal orientation determined by Laue x-ray diffraction. Most of the ESR experiments were done on $\sim 1 \times 0.5 \times 0.3 \text{ mm}^3$ single crystals in a Bruker spectrometer using a X-band (9.479 GHz) TE_{102} room- T cavity and a Q band (34.481 GHz) cool split-ring cavity, both coupled to a T -controller using a helium gas flux system for $4.2K \lesssim T \lesssim 300 \text{ K}$. $M(T, H)$ measurements for $2 \text{ K} \lesssim T \lesssim 300 \text{ K}$ were taken in a Quantum Design SQUID-RSO *dc*-magnetometer. The Eu^{2+} concentration was obtained from Curie-Weiss fits of the susceptibility data.

III. EXPERIMENTAL RESULTS

Figure 1 presents the X-band ESR spectrum of Eu^{2+} in a $\text{Ca}_{1-x}\text{Eu}_x\text{B}_6$ single crystal for $x = 0.003$ at room- T for $H \parallel [001]$. The spectrum shows the *fine* and *hyperfine* structures corresponding to seven groups ($4f^7, S = 7/2$) of twelve hyperfine resonances due to the $^{151}\text{Eu}^{2+}$ (47.8%; $I = 5/2$) and $^{153}\text{Eu}^{2+}$ (52.2%; $I = 5/2$) isotopes. The line shape of the individual resonances is Lorentzian as expected for an *insulating* environment for the Eu^{2+} ions, in agreement with the spectrum reported for $x \lesssim 0.001$ (see Fig. 2b in Ref. [9]). The angular dependence of the *fine* structure (seven groups of twelve hyperfine resonances) for the field rotated in the (110) plane is shown in the inset of Fig. 1. This angular dependence was simulated using the spin Hamiltonian $H = g\beta\mathbf{H}\cdot\mathbf{S} + (b_4/60)(\mathbf{O}_4^0 + 5\mathbf{O}_4^4) + (b_6/1260)(\mathbf{O}_6^0 - 21\mathbf{O}_6^4)$. The first term is the Zeeman interaction and the second and third ones are the cubic CF terms.[27] The isotropic hyperfine coupling, $A\mathbf{I}\cdot\mathbf{S}$, is not included in the simulation, which yielded the following values for the spin Hamiltonian parameters: $g = 1.988(4)$, $b_4 = -38.5(5)$ Oe, and $b_6 \lesssim 2(1)$ Oe. The hyperfine parameters, $^{151}A = 35.2(4)$ Oe and $^{153}A = 15.8(4)$ Oe, were obtained from simulations of twelve hyperfine resonances within the $1/2 \leftrightarrow -1/2$ spin transition of the spectrum for $H \parallel [001]$.

Figure 2 presents the X-band ESR spectra of Eu^{2+} in $\text{Ca}_{1-x}\text{Eu}_x\text{B}_6$ single crystals with $0.003 \leq x \leq 1.00$ at room- T and $H \parallel [001]$. The data show that the individual resonances and the spectra, as a whole, become broader as x increases. Nonetheless, the Eu^{2+} resolved *fine* structure is still observed up to Eu concentrations of the order of $x \approx 0.15$. This is in contrast to Gd^{3+} in $\text{Ca}_{1-x}\text{Gd}_x\text{B}_6$, where a Gd concentration of just $\sim 0.1 - 0.2\%$ is sufficient to collapse the entire spectrum into a single *metallic* narrow line.[9] The *fine* structure for the crystals with $x = 0.07, 0.10$ and 0.15 also show the angular dependence corresponding to a CF of cubic symmetry. The corresponding spin Hamiltonian parameters are given in Table I.

Figures 3a and 3b display the room- T angular dependence of the X band ESR peak-to-peak line width, ΔH , for the sample with $x = 0.15$ for the field rotated in the (110) and (100) planes, respectively. ΔH was estimated by fitting the spectra to a single Dysonian line that *averages* the shape of the spectra. Although this method yields only a rough estimate of ΔH , it provides an accurate account of the relative changes in ΔH . The angular variation observed with X band corresponds to a CF of cubic symmetry.[28, 29, 30] The solid lines are the fitting of the data to $\Delta H = a + b | 1 - 5\sin^2(\theta) + \frac{15}{4}\sin^4(\theta) |$ and $\Delta H = a + b | 1 - \frac{5}{4}\sin^2(2\theta) |$ for the (110) and (100) planes, respectively.[27] The fitting parameters are $a = 276(5)$ Oe and $b = 72(5)$ Oe. For $x \gtrsim 0.30$ the spectra show a single Dysonian resonance with no resolved *fine* structure. For these crystals the angular dependence of ΔH presents a minimum at [111] when the

field is rotated in the (110) plane, and a minimum along the [110] direction when the field is rotated in the (100) plane. This behavior is shown in Figs. 3c and 3d for $x = 0.30$ and indicates that the origin of the line width anisotropy is not due to a CF of cubic symmetry. Similar behavior was found for the samples with $x = 0.60$ (not shown here) and $x = 1.00$ (see Ref.[26] and Figs. 6 and 7 below). The solid lines are the fitting of the data to $\Delta H^2(\theta, \phi) = A + Bf_4(\theta, \phi) + Cf_6(\theta, \phi)$ for the angular dependence in the (110) and (100) planes. The functions $f_4(\theta, \phi)$ and $f_6(\theta, \phi)$ are the linear combinations of spherical harmonics of fourth and sixth order having cubic symmetry.[31] The parameters A , B and C depend on H and T , and for the present data we found $A = 423(2)$ kOe, $B = 2.3(5)$ kOe and $C = -0.03(2)$ kOe.

Figures 4a, 4b and 4c display the Q-band spectra at room- T for the $x = 0.07, 0.10$, and 0.15 samples of Fig. 2. Since the fits in Figs. 3a and 3b using a single line are not completely satisfactory, we simulate the experimental spectra in Fig. 4 as the superposition of two different Eu²⁺ ESR spectra: a spectrum with resolved *fine* structure of Lorentzian resonances (*fSL*) corresponding to Eu²⁺ ions in *insulating* media, and a Dysonian (*D*) resonance associated to Eu²⁺ ions in a *metallic* environment. For $x \gtrsim 0.30$, however, the spectra are well fitted by a single Dysonian resonance with nearly the same *g*-value and increasing line width as x increases (see Fig. 4d). The fits in Figs. 4a, 4b and 4c are a crude simulation for the coexistence of two different local environments for the Eu²⁺ ions in the region $0.07 \lesssim x \lesssim 0.15$.

Figures 5a and 5b present the angular dependence of ΔH in the (110) plane for the $x = 0.10$ and 0.15 samples at room- T measured with X and Q bands. The data is analyzed as in Figs. 3a and 3b in terms of a single resonance. The angular dependence indicates that, for these two samples, there are two competing contributions to ΔH , one due to the unresolved CF *fine* structure of cubic symmetry and a second one of lower symmetry which is more evident for Q band. The solid lines are fittings of ΔH using a weighted superposition of these two contributions, i.e. $\Delta H = \tilde{a} + \tilde{b} | 1 - 5 \sin^2(\theta) + \frac{15}{4} \sin^4(\theta) | + [\tilde{A} + \tilde{B}f_4(\theta, \phi) + \tilde{C}f_6(\theta, \phi)]^{1/2}$. The fitting parameters are given in Table II. Within the accuracy of the measurements, the samples with $x \leq 0.07$ did not show significant differences in the *fine* structure spectra between X and Q bands.

The angular dependence of ΔH measured at X and Q bands in the (110), (100) and (001) planes is shown for $x = 0.30$ at 297 K and 50 K in Fig. 6, and for $x = 1.00$ at 297 K and 150 K in Fig. 7. Note that (1) ΔH becomes smaller and more anisotropic at high fields (Q band), and (2) within the accuracy of the measurements, the narrowing and anisotropy is nearly independent of temperature for $T \gtrsim 100$ K.

For the same samples of Fig. 2, Fig. 8 displays the room- T X band ESR spectra for the magnetic field in the (110) plane along the angle of minimum ΔH , i.e. $\sim 30^\circ$ ($\sim 55^\circ$) away from the [001] direction for $x \leq 0.15$

($x \geq 0.30$). The data show the increase of ΔH as x increases. For x between 0.07 and 0.15 the line shape can be approximated as an admixture of Lorentzian and Dysonian (see Fig. 4). For $x \geq 0.30$ the line shape is purely Dysonian with a $A/B \approx 2.3$ ratio corresponding to a skin depth much smaller than the size of the crystals.[32] The Dysonian line shape suggests a *metallic* environment for the Eu²⁺ ions, confirming an increasing *semimetallic* character of Ca_{1-x}Eu_xB₆ as x increases.

Figure 9a displays ΔH for the spectra of Fig. 8 measured at X and Q bands. For the Eu²⁺ ions in the *metallic* environment, ΔH becomes narrower at higher fields (Q band). Fig. 9b shows the line width anisotropy, ${}^{Q,X}\Delta H_{[001]} - {}^{Q,X}\Delta H_{\min}$, which is larger for the Q band than for the X band. Fig. 9c shows that the line width reduction, ${}^Q\Delta H_{\min} - {}^X\Delta H_{\min}$, is nearly x -independent in the metallic regime (see Figs. 5, 6 and 7). This behavior suggests that the Eu²⁺-Eu²⁺ dipolar interaction cannot be responsible for the concentration broadening of the Eu²⁺ resonance shown in Figs. 2 and 8.[33]

Figures 10a and 10b present, respectively, the T -dependence of ΔH and the *g*-value measured at X band. Here H lies in the (110) plane and is oriented along the angle of minimum ΔH , i.e. $\sim 30^\circ$ ($\sim 55^\circ$) away from the [001] direction for $x \leq 0.15$ ($x = 0.30$ and 0.60). Note that above ~ 50 K and for $x \geq 0.30$ both, ΔH and *g* are T -independent. There is a dramatic increase in both *g* and ΔH for x between 0.15 and 0.30. The broadening of the resonance and the increase of the *g*-value for $x \gtrsim 0.30$ and $T \lesssim 30$ K indicates that there are short range ferromagnetic correlations already in the paramagnetic phase ($T \gtrsim T_c$).

The *g*-values and CF parameters, b_4 , measured for the low concentration crystals, are listed in Table I. As usual for insulators, we found a T -dependent b_4 . For $x = 0.003$ we measured a decrease of about 5% in $|b_4|$ when the temperature is raised from ~ 10 K to ~ 300 K. This T -dependence is actually expected from the thermal expansion of the lattice.[27, 34, 35] In addition, within the accuracy of the measurements $|b_4|$ for $x = 0.15$ is about the same as for $x = 0.003$. This is also not unexpected, since the lattice parameter does not significantly change with x .

IV. ANALYSIS AND DISCUSSION

The spectra of Eu²⁺ in Ca_{1-x}Eu_xB₆ presented in this paper can be classified into three different concentration regimes. (1) For $x < 0.07$ the resonance line shapes are Lorentzian and, therefore, the local environment of the Eu²⁺ sites is *insulating*. As a consequence of the relatively slow spin-lattice relaxation, the *fine* and *hyperfine* structures are fully resolved in this regime. From the isotropic *g*-value ($\approx 1.988(4)$) and the anisotropy of the *fine* structure it is inferred that the local symmetry is cubic (see Fig. 1). (2) For $0.07 \leq x \leq 0.15$ the ESR spectra can be interpreted as a superposition of a resolved *fine*

structure (*f*SL) and a Dysonian (*D*) resonance (see Fig. 4). The angular dependence of the *averaged* line width corresponds to a superposition of two competing contributions, one due to an unresolved CF of cubic symmetry and a second one with overall cubic symmetry due to three equivalent tetragonal contributions along the three [001] axes (see Figs. 2, 3, 4 and 5). The *g*-values are isotropic, within the accuracy of our measurements. In this regime the ESR line shape begins to show a Dysonian shape, i.e. it starts to display *metallic* character (see Fig. 8). Here the microwave skin depth became comparable to the size of our crystals ($\sim 1 \times 0.5 \times 0.3$ mm³). (3) For $x \geq 0.30$ the Eu²⁺ ESR line shape is purely Dysonian, i.e., there is spin diffusion and the local environment is *metallic*. The *fine* and *hyperfine* structures can no longer be resolved and the *g*-value and ΔH are *T*-independent down to ~ 30 K (see Figs. 10a and 10b).

The absence, or negligible, linear *T*-broadening of ΔH (*Korringa* relaxation) for $x \gtrsim 0.3$ is a consequence of the very low carrier density in these systems. Also, a strong *q*-dependence of the exchange interaction, $J(q)$, ($q = |k_f - k_i|$, conduction electron momentum transfer) leading to a small average exchange interaction over the Fermi surface, $\langle J^2(q) \rangle_{FS}$, could in part be responsible for this behavior. The larger *g*-values observed for the samples with $x \geq 0.30$ also suggest a strong *q*-dependence of the exchange interaction.[36] At low *T* a strong shift and broadening can be observed due to ferromagnetic short range Eu²⁺-Eu²⁺ correlations (see Figs. 10a and 10b). The minimum in ΔH at $\sim 55^\circ$ when the field is rotated in the (110) plane and at 45° when it is rotated in the (100) plane (see Figs. 3c and 3d) suggests the presence of simultaneous tetragonal components along each of the three [001] axes, that average to a cubic symmetry. However, within the accuracy of our measurements, a weak trigonal component can not be excluded. This lower symmetry of the Eu²⁺ site is observed in the line width.

In the small *x* limit, each Eu²⁺ represents a charge neutral substitution, which gives rise to a bound state in the gap of the semiconductor, as a consequence of the broken translational invariance. The impurity states are localized within the extension of about an unit cell. As the number of impurity states increases with *x*, they start to overlap and eventually form a *percolative* network. The critical concentration for nearest neighbor site *percolation* on a simple cubic lattice is $x_c = 0.307$.[37] The *percolation* threshold is reduced to $x_c = 0.137$ if next-to-nearest neighbors are included, which correspond to neighbors in the [110]-directions. Third neighbors are along the diagonals of the cube, but this direction is blocked for the wave functions because of the large B₆²⁻ anions. From our results, it is reasonable to assume that the transition from *insulator* to *metal* occurs at an Eu concentration of about 14%. Hence, assuming a homogeneous distribution of Eu, for $x < x_c$ the system is *insulating* and the *fine* and *hyperfine* structures could be resolved. The data at room-*T* shows a gradual broadening of the individual Eu²⁺ resonances with increasing *x* (see Figs. 2

and 4). We argue that this cannot be attributed to Eu²⁺-Eu²⁺ magnetic correlations because the *g*-value and ΔH are *T*-independent (see Figs. 10a and 10b for $x < x_c$). Thus, the broadening for $x \leq 0.15$ may be attributed to site symmetry breaking due to Ca/Eu substitution. This inhomogeneous broadening is probably responsible for hiding the Eu²⁺ *fine* and *hyperfine* structures as *x* increases. Weak or no *T*-dependence is expected from this inhomogeneous broadening.

For $x > x_c$, on the other hand, the system is *metallic* and spin-diffusion can take place, giving rise to a Dysonian line shape. With increasing *x* the impurity band gradually smears the semiconducting gap at the *X*-points of the Brillouin zone and the system evolves to a *semimetal* for *x* = 1 (EuB₆).[18] EuB₆ orders FM at $T_c \approx 15.3$ K,[22, 38] indicating the existence of short and long range Eu²⁺-Eu²⁺ magnetic correlations around T_c . At T_c , EuB₆ undergoes a transition into a *metallic* state at low *T* with an increase of the number of carriers and/or a decrease of their effective mass.[17, 23, 39] This transition is believed to be associated with the formation of magnetic polarons, i.e. the spin of a conduction electron polarizes the Eu²⁺-spin in its neighborhood and drags this polarization cloud as it moves. Note that due to the *semimetallic* character there are many more Eu²⁺-spins than conduction electrons. The magnetic correlations increase as *T* is reduced, so that the size of the polarization clouds increases, they eventually overlap and a FM state is obtained. The transition into a FM state is foreseen in the ESR spectra (see Fig. 10). The *g*-values and ΔH are independent of *T* down to 50 K for all *x*. However, for $x \gtrsim 0.30$ and $T \lesssim 50$ K there is a significant *T*-dependence. The *g*-value strongly increases due to the FM correlations (polarons and FM short-range order). These correlations clearly increase with *x* and decreasing *T*. ΔH also increases when the short-range order sets in due to the generation of magnons.

For crystals with $x \gtrsim 0.30$ the angular dependence of ΔH has an overall cubic symmetry that corresponds to a superposition of three tetragonal environments. There are two possible scenarios to explain these findings. Within the first scenario, the origin for the tetragonal symmetry may be associated with the Eu/Ca substitution. This scenario assumes that the CF of an Eu²⁺ ion is determined by the nearest neighbor cation ions. If an Eu ion is surrounded by five Eu and one Ca, the local symmetry is tetragonal. Since the Ca ion can be along any one of the axis, there is a superposition of tetragonal symmetries along the three directions. The overall symmetry is then cubic and the spectra inhomogeneously broadened by three tetragonal angular dependence. Also, more than two Ca neighbors can give rise to a trigonal component in the line width, which was not observed. If such component is present its value is much smaller than the tetragonal contribution. However there is a concern with this scenario. This mechanism does not account for the angular dependence of stoichiometric EuB₆. It would require a much larger number of B₆ vacancies than the

claimed for these samples to explain the tetragonal dependence of ΔH .[40]

In a second possible scenario, we consider the relaxation of the Eu^{2+} -spins into the conduction electron bath and the concomitant spin-diffusion. The conduction electrons occupy three small ellipsoidal pockets centered at the X -points of the Brillouin zone, i.e., at $(\pm\pi/a, 0, 0)$, $(0, \pm\pi/a, 0)$ and $(0, 0, \pm\pi/a)$,[41] where a is the lattice constant. The drift of the diffusion is then predominantly into the direction of the major axis of the ellipsoids, i.e. along one of the axis of the cube. Thus, each relaxation process gives rise to a tetragonal angular dependence of ΔH . The superposition of the relaxation into the three directions is then cubic. This mechanism explains why there is a tetragonal dependence in the *metallic* regime but not in the *insulating* one. Finally, the mechanism also applies to stoichiometric EuB_6 . For EuB_6 , Urbano *et al.* [26] have attributed the broad ESR line to a homogeneous resonance, where the main contribution to ΔH involves a spin-flip scattering relaxation process due to the exchange interaction between the conduction and Eu^{2+} 4f-electrons.

The exchange J of the order of 0.15 eV is much larger than the thermal energy and locally binds the conduction electrons to the Eu^{2+} spins. The relaxation process is then essentially T -independent for $T > 50$ K. The exchange $J(r)$ strongly decreases with the distance between the conduction electron and Eu^{2+} ion. At lower T , the thermal energy is less than the exchange with more distant Eu ions, thus allowing the formation of larger polarons, which eventually give rise to ferromagnetism. The H , T and angular-dependence of the measured ΔH lead to the conclusion that magnetic polarons and Fermi surface effects dominate in the spin-flip scattering of EuB_6 .

Experimental support for the second scenario comes from the ESR data and the magnetoresistance. Figs. 5, 6 and 7 show that the high field ESR spectra present narrower and more anisotropic lines for $x \gtrsim 0.30$, indicating that ΔH is predominantly determined by a spin-flip scattering process. This situation is similar to EuB_6 . Furthermore, the negative magnetoresistance observed in $\text{Ca}_{1-x}\text{Eu}_x\text{B}_6$ for $x \gtrsim 0.30$ also supports the presence of magnetic polarons in these systems.[23, 24, 42] Moreover, even in the percolative region, $0.10 \lesssim x \lesssim 0.15$, our data support this second scenario. The results of Fig. 5 clearly show that there are two competing contributions to the Eu^{2+} ESR line width. One corresponds to the *inhomogeneous* broadening of unresolved CF *fine* structure of cubic symmetry and the other one is associated with the *homogeneous* broadening caused by the spin-flip scattering. The latter has components of tetragonal symmetry along the three axis with an overall cubic dependence (see above). As x increases, the homogeneous spin-flip scattering contribution to ΔH starts to overcome the inhomogeneous broadening due to CF effects. For $x \gtrsim 0.30$, the mobility of the carriers increases with increasing x (a more connected network of impurity bound states), enhances the spin-diffusion and contributes to the homo-

geneous concentration broadening of ΔH . In a recent electron microscopy study Wigger *et al.* [42] found that their $x \approx 0.27$ sample presented separated regions rich in Ca^{2+} (*insulating*) and Eu^{2+} ions (*semimetallic*). According to these results, we may associate the two contributions to ΔH with regions rich in Ca^{2+} and Eu^{2+} ions, respectively. In other words, we associate the *fSL* in Fig. 4 with regions rich in Ca^{2+} and the *D* resonance with regions rich in Eu^{2+} , although in reality a distribution of resonances, rather than just two, should be considered.

The situation is actually quite similar to the case of $\text{Ca}_{1-x}\text{Gd}_x\text{B}_6$, where coexistence of *insulating* and *metallic* regions were inferred from the Gd^{3+} ESR spectra, although, at much lower concentrations.[9] Therefore, the collapse of the CF *fine* structure found in $\text{Ca}_{1-x}\text{Gd}_x\text{B}_6$ is also observed in the $\text{Ca}_{1-x}\text{Eu}_x\text{B}_6$ system.

With respect to the controversial scenario of the conductivity of stoichiometric CaB_6 , the Eu^{2+} ESR results in $\text{Ca}_{1-x}\text{Eu}_x\text{B}_6$ for $x < 0.07$ and those in $\text{Ca}_{1-x}\text{R}_x\text{B}_6$ ($\text{R} = \text{Gd}^{3+}$, Er^{3+}) for $x \lesssim 0.001$,[9] reveal an *insulating* local environment for the dopants, Eu^{2+} , Gd^{3+} and Er^{3+} , supporting that pure CaB_6 is a “wide-gap” semiconductor. Regarding the reported sample dependence for R -doped CaB_6 , we would like to point out that in our study neither the Eu^{2+} ESR spectra nor the $M(H)$ data in $\text{Ca}_{1-x}\text{Eu}_x\text{B}_6$ were found to be sample dependent. However, there is a strong sample dependence in the ESR spectra of (Gd, Er)-doped CaB_6 for concentrations of $\sim 0.1 - 0.2\%$. This can probably be attributed to the donor states with large extension provided by the Ca/Gd and Ca/Er substitution.

All our crystals presented a WF component $\lesssim 0.5$ emu/mole, i.e., smaller than those for La-doped CaB_6 crystals grown using the same method.[1, 9] Furthermore, for $x \gtrsim 0.10$, the WF component became difficult to measure due to the large M of Eu^{2+} . The above results suggest that the WF is probably caused by self-doping or extrinsic impurities which are inherent to the employed materials and crystal growth techniques.

V. CONCLUSIONS

In summary, we report ESR results in $\text{Ca}_{1-x}\text{Eu}_x\text{B}_6$. As a function of Eu concentration, an evolution from *insulating* to *semimetallic* character is observed from the change in the line shape of the Eu^{2+} ESR spectra. The gradual transition between these two regimes is estimated to occur at $0.10 \lesssim x \lesssim 0.20$, indicating that a next-to-nearest neighbor *site percolation* network of Eu^{2+} bound states is the origin of this evolution. In analogy to $\text{Ca}_{1-x}\text{Gd}_x\text{B}_6$ [9] a coexistence of *insulating* and *metallic* regions was found for Eu concentrations in the *percolative* transition regime. However, the collapse of the CF *fine* structure is found at a much larger of Eu concentration, because, in contrast to Gd^{3+} , Eu^{2+} does not provide donor carriers. The dramatic variation of ΔH and the g -value at the percolative transition revealed by our ESR

data is attributed to change in the electron mobility at these concentrations. From the ESR data for $x \leq 0.15$ we extracted the Eu²⁺ spin Hamiltonian parameters.

For crystals with Eu concentration above the *percolative* region ($x \gtrsim 0.15$) the line width shows: (i) a field narrowing, which arises from magnetic polarons,[26] (ii) an angular dependence that corresponds to the superposition of three tetragonal components along the [001] axes, and is related to the relaxation mechanism and the Fermi surface,[26] and (iii) a broadening with the Eu concentration, which is attributed to an enhanced spin-flip relaxation caused by the increased mobility of the carriers. (iv) For $x \gtrsim 0.30$ and $T \lesssim 50$ K, the broaden-

ing and shift of the ESR spectra anticipate the onset of FM correlations between the Eu²⁺ ions due to magnetic polarons. All measured Ca_{1-x}Eu_xB₆ crystals presented a WF smaller than ~ 0.5 emu/mole, i.e., much smaller than that reported by Young *et al.* [1] for La doped CaB₆.

The work at UNICAMP is supported by FAPESP and CNPq, and the work at the NHMFL by NSF Cooperative Agreement No. DMR-9527035 and the State of Florida. The support by NSF (grants Nos. DMR-0102235 and DMR-0105431) and DOE (grant No. DE-FG02-98ER45797) is also acknowledged.

[1] D.P. Young *et al.*, *Nature* **397**, 412 (1999).
 [2] M.E. Zhitomirsky *et al.*, *Nature* **402**, 251 (1999).
 [3] L. Balents and C.M. Varma, *Phys. Rev. Lett.* **84**, 1264 (2000).
 [4] V. Barzykin and L.P. Gor'kov, *Phys. Rev. Lett.* **84**, 2207 (2000).
 [5] T. Jarlborg, *Physica B* **307**, 291 (2001); *Phys. Rev. Lett.* **85**, 186 (2000).
 [6] D. Ceperley, *Nature* **397**, 386 (1999).
 [7] H. J. Tromp *et al.*, *Phys. Rev. Lett.* **87**, 16401 (2001).
 [8] S. Massidda, A. Continenza, T.M. de Pascale, and R. Monnier, *Z. Phys. B: Cond. Matter* **102**, 83 (1997).
 [9] R.R. Urbano, C. Rettori, G.E. Barberis, M. Torelli, A. Bianchi, Z. Fisk, P.G. Pagliuso, A. Malinowski, M.F. Hundley, J.L. Sarrao, and S.B. Oseroff, *Phys. Rev. B* **65**, 180407(R) (2002).
 [10] T. Moriwaka *et al.*, *J. Phys. Soc. Jpn.* **70**, 341 (2001).
 [11] D. Hall *et al.*, *Phys. Rev. B* **64**, 233105 (2001).
 [12] P. Vonlanthen *et al.*, *Phys. Rev. B* **62**, 10076 (2000).
 [13] H. R. Ott *et al.*, *Z. Phys. B* **102**, 337 (1997).
 [14] J. L. Gavilano *et al.*, *Phys. Rev. B* **63**, 140410(R) (2001).
 [15] K. Giannìo *et al.*, *J. Phys. Condens. Matter* **14**, 1035 (2002).
 [16] J.D. Denlinger *et al.*, *Phys. Rev. Lett.* **89**, 157601 (2002).
 [17] Jong-Soo Rhyee, B.K. Cho, and H.-C. Ri, *Phys. Rev. B* **67**, 125102 (2003).
 [18] S. Souma, H. Komatsu, T. Takahashi, R. Kaji, T. Sasaki, Y. Yokoo, and J. Akimitsu, *Phys. Rev. Lett.* **90**, 027202 (2003).
 [19] T. Terashima *et al.*, *J. Phys. Soc. Jpn.* **69**, 2423 (2000).
 [20] K. Matsubayashi, M. Maki, T. Tsuzuki *et al.*, *Nature* **420**, 143 (2002); Z. Fisk, *Nature* **420**, 144 (2002).
 [21] M.C. Bennett, J. van Lierop, E.M. Berkeley, J.F. Mansfield, C. Henderson, M.C. Aronson, D.P. Young, A. Bianchi, Z. Fisk, F. Balakirev, and A. Lacerda, *Phys. Rev. B* **69**, 132407 (2004).
 [22] S. Süllow *et al.*, *Phys. Rev. B* **57**, 5860 (1998).
 [23] S. Paschen *et al.*, *Phys. Rev. B* **61**, 4174 (2000).
 [24] G.A. Wigger, Ch. Walti, H.R. Ott, A.D. Bianchi, and Z. Fisk, *Phys. Rev. B* **66**, 212410 (2002); G.A. Wigger, R. Monnier, H. R. Ott, D. P. Young and Z. Fisk, *cond-mat* 0309412 (2003).
 [25] R.R. Urbano, P.G. Pagliuso, J.L. Sarrao, S.B. Oseroff, C. Rettori, A. Bianchi, S. Nakatsuji, and Z. Fisk, *J. Magn. Magn. Mater.* **272-276**, Suppl. 1, E1659 (2004).
 [26] R.R. Urbano, P.G. Pagliuso, C. Rettori, S.B. Oseroff, J.L. Sarrao, P. Schlottmann, and Z. Fisk, *Phys. Rev. B* **70**, 140401(R) (2004).
 [27] A. Abragam and B. Bleaney, *EPR of Transition Ions* (Clarendon Press, Oxford, 1970).
 [28] D. Davidov, C. Rettori and V. Zevin, *Solid State Commun.* **16**, 247 (1975).
 [29] C. Rettori, D. Davidov, A. Grayewskey and W.M. Walsh, *Phys. Rev. B* **11**, 4450 (1975).
 [30] H. Luft, K. Baberschke and K. Winzer *Z. Phys. B - Cond. Matt.* **47**, 195 (1982).
 [31] S.B. Oseroff and R. Calvo, *Phys. Rev. B* **18**, 3041 (1978).
 [32] G.E. Pake and E.M. Purcell, *Phys. Rev.* **74**, 1184 (1948); N. Bloembergen, *J. Appl. Phys.* **23**, 1383 (1952); G. Feher and A.F. Kip, *Phys. Rev.* **98**, 337 (1955); F.J. Dyson, *Phys. Rev.* **98**, 349 (1955); .
 [33] G. Sperlich and K. Jansen, *Solid State Comm.* **15**, 1105 (1974).
 [34] H.A. Buckmaster and Y.H. Shing, *Phys. Stat. Sol.(a)* **12**, 325 (1972).
 [35] M. Bartkowski, D.J. Northcott, J.M. Park, A.H. Deddoch, and F.T. Hedgecock, *Solid State Commun.* **56**, 659 (1985).
 [36] D. Davidov, K. Maki, R. Orbach, C. Rettori, and E.P. Chock, *Solid State Commun.* **12**, 621 (1973).
 [37] J.W. Essam, in *Phase Transitions and Critical Phenomena*, edited by C. Domb and M.S. Green, vol. 2, (Academic Press, London, 1972), p. 197; P. Schlottmann and C.S. Hellberg, *J. Appl. Phys.* **79**, 6414 (1996).
 [38] S. Oseroff, R. Calvo, J. Stankiewicz, Z. Fisk, and D.C. Johnston, *Phys. Stat. Sol.* **94**, K133 (1979).
 [39] M.C. Aronson, J.L. Sarrao, Z. Fisk, M. Whitton, and B.L. Brandt, *Phys. Rev. B* **59**, 4720 (1999).
 [40] Z. Fisk *et al.*, *J. Appl. Phys.* **50**, 1911 (1979).
 [41] R.G. Goodrich, N. Harrison, J.J. Vuillemin, A. Tekul, D.W. Hall, Z. Fisk, D. P. Young, and J. L. Sarrao, *Phys. Rev. B* **58**, 14896 (1998).
 [42] G.A. Wigger, C. Beeli, E. Felder, H.R. Ott, A.D. Bianchi, and Z. Fisk, *Phys. Rev. Lett.* **93**, 147203 (2004).

TABLE I: X-band room- T spin Hamiltonian parameters. The g values were measured at the minimum line width. The b_4 parameters were obtained for $H \parallel [001]$.

x (%)	g -value	b_4 (Oe)
0.3	1.988(4)	-38.5(5)
7.0	1.997(4)	-38.6(5)
10.0	2.001(5)	-39.3(5)
15.0	2.003(5)	-40.9(5)
30.0	2.03(2)	-
60.0	2.03(2)	-
100.0	2.03(3)	-

TABLE II: Room- T parameters obtained from the fittings of the angular dependence of the ESR line width in Fig. 5.

x (%)	Band	\tilde{a} (Oe)	\tilde{b} (Oe)	\tilde{A} (Oe)	\tilde{B} (Oe)	\tilde{C} (Oe)
10.0	X	245(10)	110(5)	100(20)	8(3)	3(1)
	Q	170(10)	60(6)	1400(100)	260(20)	1(1)
15.0	X	275(10)	50(5)	190(20)	50(5)	3(1)
	Q	170(10)	30(3)	2740(30)	560(10)	8(2)

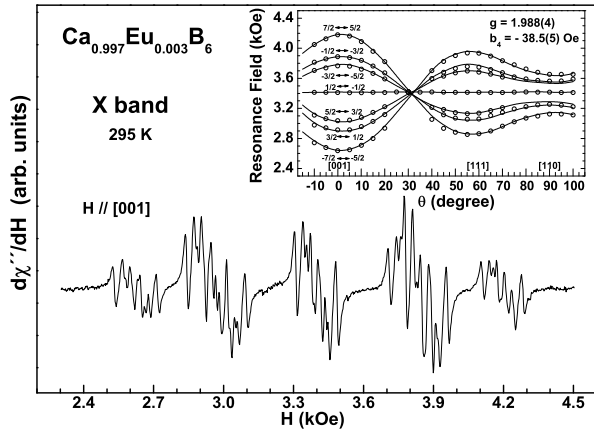


FIG. 1: X band ESR spectrum of Eu^{2+} in a $\text{Ca}_{0.997}\text{Eu}_{0.003}\text{B}_6$ single crystal at room- T with $H \parallel [001]$. Inset: Fine structure angular dependence (open circles) and simulation (solid lines) in the (110) plane.

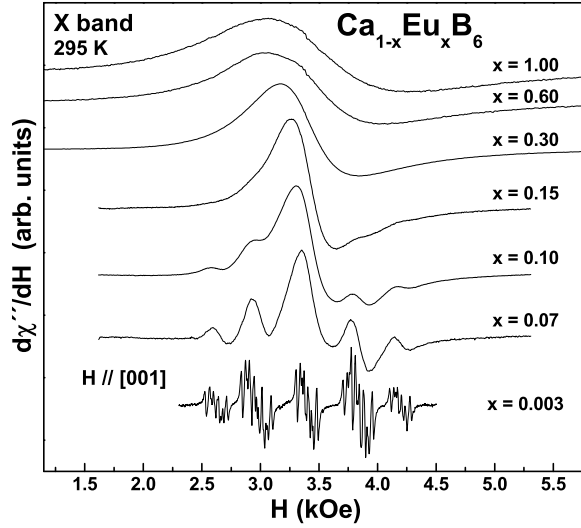


FIG. 2: ESR spectra of Eu^{2+} in $\text{Ca}_{1-x}\text{Eu}_x\text{B}_6$ single crystals for $0.003 \leq x \leq 1.00$ at room- T for $H \parallel [001]$.

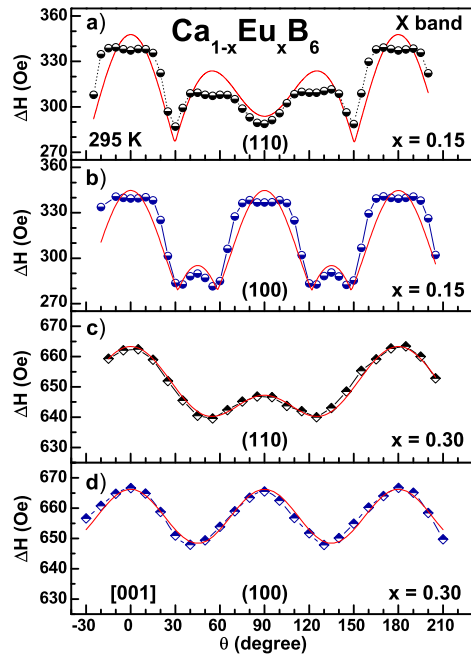


FIG. 3: (color online) Angular dependence of ΔH at room- T for $x = 0.15$ and 0.30 . An "averaged" single Dysonian line shape was used to determine ΔH . For a) and c) the angular dependence is in the (110) plane, for b) and d) in the (001) plane. The solid lines are fittings to $\Delta H = a + b |1 - 5 \sin^2(\theta) + \frac{15}{4} \sin^4(\theta)|$ for a), $\Delta H = a + b |1 - \frac{5}{4} \sin^2(2\theta)|$ for b), and $\Delta H^2(\theta, \phi) = A + Bf_4(\theta, \phi) + Cf_6(\theta, \phi)$ for c) and d) (see text). The dashed lines are a guide to the eye.

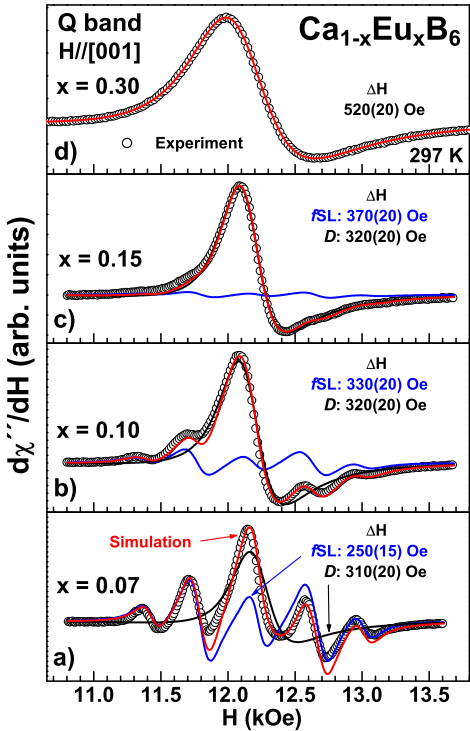


FIG. 4: (color online) Q-band ESR spectra for a) $x = 0.07$; b) $x = 0.10$; c) $x = 0.15$; and d) $x = 0.30$ at room- T and $H \parallel [001]$. The open symbols are the experimental data; f_{SL} corresponds to the cubic *fine* structure spectrum of 7 resonances (ΔH is the line width of each resonance) and D to the Dysonian resonance. In a), b) and c), the simulations of the data are given by the superposition of f_{SL} and D . In d) the simulation is given by a single Dysonian resonance (see text). The g values were found to be $g = 2.00(3)$ in all cases.

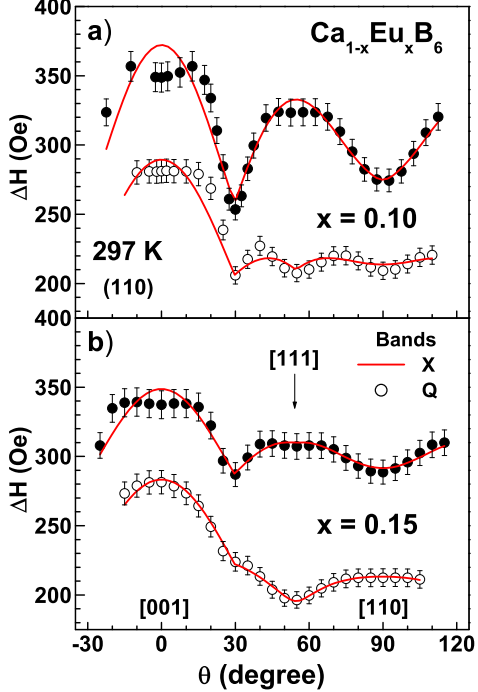


FIG. 5: (color online) X- and Q-band angular dependence of ΔH at room- T in the (110) plane: a) for $x = 0.10$, and b) $x = 0.15$. An "averaged" single Dysonian line shape was used to determine ΔH . The solid lines are fittings using $\Delta H = \tilde{a} + \tilde{b} \left| 1 - 5 \sin^2(\theta) + \frac{15}{4} \sin^4(\theta) \right| + [\tilde{A} + \tilde{B} f_4(\theta, \phi) + \tilde{C} f_6(\theta, \phi)]^{1/2}$ (see text).

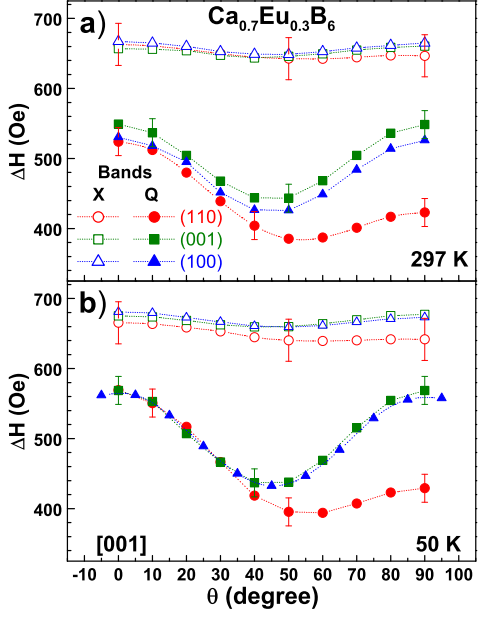


FIG. 6: (color online) Angular dependence of ΔH for X-band (open symbols) and Q-band (full symbols) in the (110), (001) and (100) planes for $\text{Ca}_{0.7}\text{Eu}_{0.3}\text{B}_6$ at a) room- T and b) 50 K.

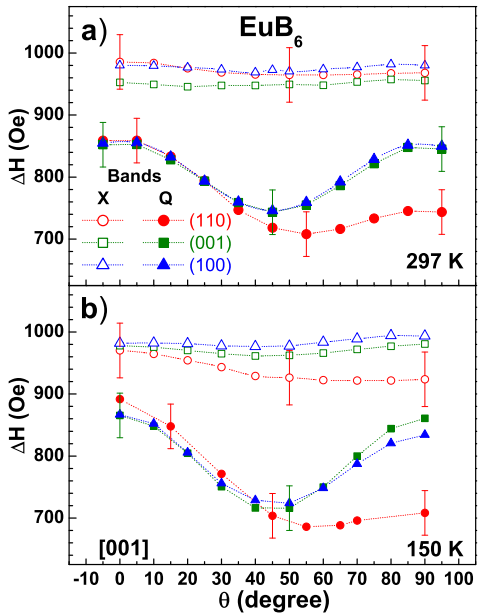


FIG. 7: (color online) Angular dependence of ΔH at X-band (open symbols) and Q-band (full symbols) in the (110), (001) and (100) planes for EuB_6 at a) room- T and b) 150 K.

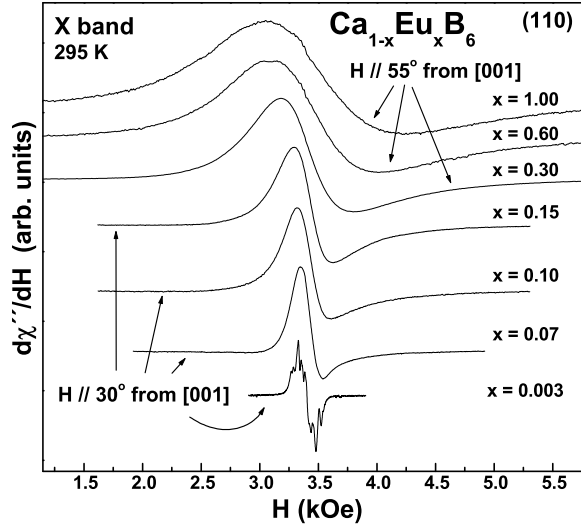


FIG. 8: ESR spectra of Eu^{2+} in $\text{Ca}_{1-x}\text{Eu}_x\text{B}_6$ single crystals at room- T with H in the (110) plane. For $0.003 \leq x \leq 0.15$, H is at 30° from [001], while for $0.30 \leq x \leq 1.00$, H is at 55° from [001].

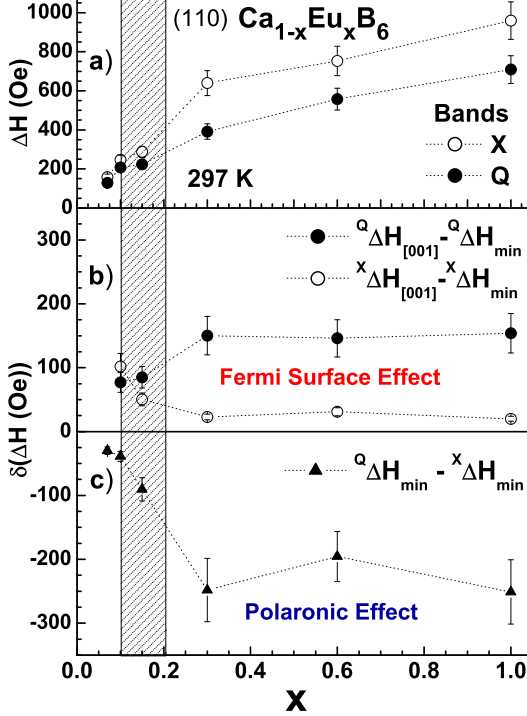


FIG. 9: (color online) H and x -dependence of ΔH at room- T : a) ${}^{X,Q}\Delta H$ for the spectra of Figure 8, b) difference between the maximum and minimum line widths, ${}^{Q,X}\Delta H_{[001]} - {}^{Q,X}\Delta H_{\min}$, and c) difference between the minimum line widths, ${}^Q\Delta H_{\min} - {}^X\Delta H_{\min}$. The gradual transition region between *insulating* and *semimetallic* environments is shown as a shaded area ($0.10 \lesssim x \lesssim 0.20$).

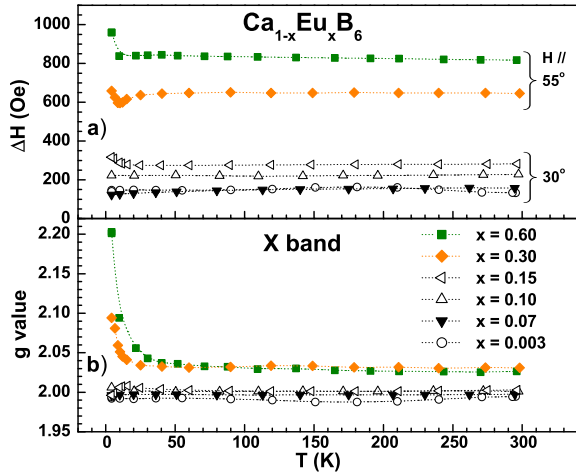


FIG. 10: (color online) X-band T -dependence of: a) the line-width ΔH , and b) the g -value, for the crystals and orientations corresponding to Figure 8.